Photometric Data from Nonresolved Objects for Improved Drag and Reentry Prediction

Piyush M. Mehta* and Richard Linares†
University of Minnesota, Minneapolis, Minnesota 55455-0153
and
Andrew C. Walker‡
Los Alamos National Laboratory, Los Alamos, New Mexico 87545

DOI: 10.2514/1.A33825

Debris objects such as rocket bodies can pose a threat to active space assets in orbit and to assets and humans on the ground through reentry. Orbit and reentry predictions for low-perigee resident space objects are strongly influenced by atmospheric drag. Such predictions are typically performed using fixed or fitted drag/ballistic coefficients that can result in large prediction errors. Accurate drag coefficients require, among other things, knowledge of the attitude. This paper develops an approach to compute accurate drag coefficients for debris objects toward accurate orbit and reentry predictions. The method uses a nonlinear least-squares estimator to estimate the attitude and angular velocities using light curves for debris objects with known shape models. This paper focuses on rocket bodies in particular. The estimated attitude and angular velocities are then used to compute the drag coefficients using a flat-plate panel method. The technique is validated using simulated data scenarios with a number of representative rocket body models. Good performance is observed for the developed approach. Results show that neglecting attitude variations for resident space objects in highly elliptic orbits can result in orbit errors of more than 100 km after just ten brief passes through the atmosphere.

Nomenclature

A	=	quaternion mapping matrix from inertial to body frame
$\mathcal{A}$	=	projected area, m^2
a	=	semimajor axis, km
$\boldsymbol{a}_{\text{drag}}$	=	acceleration due to drag, $kg \cdot m \cdot s^{-2}$
BC	=	ballistic coefficient, $m^2 \cdot kg^{-1}$
b_i	=	vertices of ith triangular facet, m
$\mathcal{C}_A$	=	body axial force coefficient
$\mathcal{C}_{D,\text{ads}}$	=	adsorbate covered surface drag coefficient
$\mathcal{C}_D$	=	drag coefficient
$\mathcal{C}_{D,\text{overall}}$	=	overall drag coefficient
$\mathcal{C}_{D,T}$	=	total drag coefficient
$\boldsymbol{C}_f$	=	force coefficient
$\mathcal{C}_N$	=	body normal force coefficient
$\mathcal{C}_P$	=	pressure coefficient
$\mathcal{C}_S$	=	body side force coefficient
$\mathcal{C}_{D,s}$	=	clean surface drag coefficient
$\mathcal{C}_\tau$	=	shear coefficient
d_i, l_i	=	sides of ith triangular facet, m
e	=	eccentricity
F	=	photon flux, $W \cdot m^{-2}$
F_{obs}	=	fraction of visible light reflecting off resident space object surface
F_{reflect}	=	Fresnel reflectance
F_{sun}	=	fraction of visible light striking resident space object surface
$\boldsymbol{f}$	=	dynamic model
$\boldsymbol{g}$	=	measurement model
H	=	Jacobian matrix
$\boldsymbol{h}$	=	measurement function
inc	=	inclination, deg/rad
J	=	inertia matrix
K_L	=	Langmuir fitting constant, Pa^{-1}
K_s	=	Goodman model coefficient
k_B	=	Boltzmann constant, $m^2 \cdot kg \cdot s^{-2} \cdot K^{-1}$
L	=	cost function
M	=	number of neutral chemical species in atmosphere
M_0	=	mean anomaly
m	=	mass, kg
m_{app}	=	apparent brightness magnitude
m_{avg}	=	average mass of gas, kg
m_p	=	particle mass, kg
N	=	number of triangular facets
$\boldsymbol{n}$	=	uncorrelated measurement errors
$n_{u,v}$	=	bidirection reflectance distribution function model parameters
P	=	covariance
P_{Ox}	=	partial pressure of atomic oxygen
$\boldsymbol{q}$	=	quaternion
R_{diff}	=	diffuse reflectance coefficient
R_{spec}	=	specular reflectance coefficient
s	=	speed ratio
T_w	=	surface temperature, K
T_∞	=	freestream atmospheric temperature, K
$\boldsymbol{u}_h^I$	=	unit vector halfway between sun and observer in inertial frame
$\boldsymbol{u}_n^B$	=	unit normal vector in body frame
$\boldsymbol{u}_n^I$	=	unit normal vector in inertial frame
$\boldsymbol{u}_{\text{obs}}^I$	=	unit vector from space object to observer in inertial frame
$\boldsymbol{u}_{\text{sun}}^I$	=	unit vector from space object to sun in inertial frame
$\boldsymbol{u}_t^B$	=	unit tangential vector in body frame
$\boldsymbol{u}_{u,v}^B$	=	unit basis vector in body frame
$\boldsymbol{u}_{u,v}^I$	=	unit basis vector in inertial frame
$\boldsymbol{u}_{v_{\text{rel}}}^B$	=	unit velocity vector in body frame
v	=	facet vertices
v_{mp}	=	most probable speed, $m \cdot s^{-1}$
$\boldsymbol{v}_{\text{rel}}$	=	velocity relative to the atmosphere, $m \cdot s^{-1}$

Received 5 December 2016; revision received 24 January 2018; accepted for publication 10 February 2018; published online 20 April 2018.

*Research Associate, Department of Aerospace Engineering and Mechanics, 107 Akerman Hall, 110 Union Street Southeast. Associate Member AIAA.

†Assistant Professor, Department of Aerospace Engineering and Mechanics, 107 Akerman Hall, 110 Union Street Southeast.

‡Research Scientist, Space Science and Application, MS D466.

$\boldsymbol{x}$ = state vector
$\tilde{\boldsymbol{y}}$ = measurement vector
Z = z-score
$\tilde{\boldsymbol{z}}$ = measurements
α = total energy accommodation coefficient
α_n = normal energy accommodation coefficient
α_s = clean surface energy accommodation coefficient
α_t = tangential energy accommodation coefficient
β = bidirectional reflectance distribution functions
γ = aerodynamic pitch angle in body frame, deg/rad
δ = Dirac delta function
ϵ = convergence tolerance or residual
η = bidirection reflectance distribution function model exponent
Θ = fraction of surface coverage
θ = local flow inclination angle, deg/rad
μ = incident to surface particle mass ratio
$\boldsymbol{\xi}$ = Euler angles, deg/rad
$\boldsymbol{\Phi}$ = state transition matrix
ϕ = solution flow
ρ = atmospheric mass density, $\mathrm{kg} \cdot \mathrm{m}^{-3}$
σ_n = normal momentum accommodation coefficient
σ_t = tangential momentum accommodation coefficient
χ = mole fraction
ψ = aerodynamic yaw angle in body frame, deg/rad
Ω = right ascension of the ascending node, deg/rad
ω = argument of perigee, deg/rad
$\boldsymbol{\omega}_r$ = rotational rate, $\mathrm{deg} \cdot \mathrm{s}^{-1}$

I. Introduction

THE United States Space Surveillance Network, operated under the United States Strategic Command, faces the unique challenge of tracking more than 22,000 resident space objects (RSOs) and providing critical collision avoidance warnings to the military, NASA, and commercial operators. However, because of the large number of RSOs and the limited number of sensors available to track them, it is impossible to maintain persistent surveillance. Observation gaps result in large propagation intervals between measurements and close approaches. The observation gaps coupled with nonlinear RSO dynamics result in difficulty with modeling the probability distribution functions for the expected state of the RSO. In particular, RSOs that traverse the low-Earth-orbit (LEO) environment are heavily influenced by atmospheric drag, which is difficult to model accurately.

In this paper, we develop a new method that uses nonresolved photometric data to estimate the attitude and rotational rates of nonresolved rocket bodies, which are then used to compute time-varying drag coefficients C_D for accurate orbit prediction. Nonresolved photometric data have been studied as a mechanism for space object characterization. Photometry is the measurement of an object's flux or apparent brightness measured over a wavelength band. The temporal variation of photometric measurements is referred to as the photometric signature or light curves. The optical photometric signature of an object contains information about shape, attitude, size, and material composition [1–7]. Light-curve techniques have been used to estimate the shape and state of asteroids [8,9]. The work of Calef et al. [10] uses light curves and thermal emissions to recover the three-dimensional shape of an object, assuming its orientation with respect to the observer is known. The benefits of using a light-curve-based approach over the radar- and/or imaging-based techniques is that it is not limited to large objects in lower orbits and it can be applied to small and dim objects in higher orbits, such as geosynchronous orbits. Here, we use light-curve data because they provide a mechanism to estimate both attitude as well as rotational rates [1–7].

Atmospheric drag can add large uncertainties to the predicted state of the RSO and cause significant inaccuracies in the conjunction assessments. In the context of space situational awareness, atmospheric drag is the largest source of uncertainty in accurately predicting the orbits and reentry of RSOs that traverse the LEO environment. The large uncertainties in orbit and reentry predictions can also influence mission design in terms of predicted lifetime and fuel requirements. In addition, large nonresolved debris objects such as rocket bodies have a higher probability of surviving the harsh reentry environment. The surviving parts can contain hazardous radioactive materials or unused hydrazine that can cause damage and casualties within a populated area. Predicting reentry also has military applications. The uncertainties are derived mainly from mismodeling of the drag coefficient and atmospheric mass density [11]. The theoretical model used for drag calculations is

$$\boldsymbol{a}_{\mathrm{drag}} = -\frac{1}{2}\rho\frac{C_D\mathcal{A}}{m}v_{\mathrm{rel}}^2\frac{\boldsymbol{v}_{\mathrm{rel}}}{|\boldsymbol{v}_{\mathrm{rel}}|} \tag{1}$$

where $\boldsymbol{a}_{\mathrm{drag}}$ is the acceleration due to drag, ρ is the atmospheric mass density, C_D is the drag coefficient, $\mathcal{A}$ is the projected area perpendicular to the velocity direction, m is the mass, and $\boldsymbol{v}_{\mathrm{rel}}$ is the velocity of the RSO relative to the atmosphere.

The C_D has a direct impact on orbit prediction through the drag model. The errors are caused due to the use of inaccurate and nonphysical (fixed and fitted) C_D. Conjunction assessments and reentry predictions are typically performed using either fixed or fitted C_D. A set of observations, typically made using a radar or telescope, over several orbits or days is used to compute fitted ballistic coefficients (BCs), defined as $C_D\mathcal{A}/m$. The fitted BCs are then used to propagate the orbit through observation gaps, sometimes over a long period of time. This propagation using fitted BCs can result in large errors in orbit and reentry predictions. Accurate estimates of C_D are essential in reducing orbit and reentry prediction errors, which in turn require knowledge of the attitude and the associated rotational rates.

A fixed C_D value of 2.2 was derived and used for compact satellites early in the Space Age [12]. This derived value has been regularly applied to RSOs with complex geometry because of the resulting simplification in the analysis of the drag data. For high-aspect-ratio objects such as rocket bodies, there can be a large amount of shear that can drastically increase the C_D. Fitted C_D can account for variations due to altitude and solar conditions but do not account for the small-scale temporal variations along the orbit. Physical C_D, characterized by the interaction between the atmosphere and the object, are determined by the exchange of energy and momentum between the atmospheric molecules and the RSO surface.

Early models for atmospheric mass density were derived from the orbital decay of satellites observed and averaged over several orbits using fixed C_D to simplify the analysis [12]. Several atmospheric models, such as Naval Research Laboratory Mass Spectrometry and Incoherent Scatter Extended (NRLMSISE-00) [13] and the High Accuracy Satellite Drag Model (HASDM) [14], have been developed and used over the last decades; however, they are semi-empirical in nature and do not account for many of the complex physical phenomena that drive variations in the upper atmosphere. First-principles-based physical models of the upper atmosphere, such as the Global Ionosphere Thermosphere Model [15] and Thermosphere–Ionosphere–Electrodynamics General Circulation Model [16], offer a higher-fidelity approach but require calibration and validation and are expensive to evaluate.

HASDM, the current Air Force standard, is based on observation of calibration satellites. These satellite observations are used to estimate corrections to atmospheric model parameters in real time based on their orbit determination solutions. The corrections can be estimated as frequently as every 3 h [14]. Orbits passing within the atmosphere are perturbed by a number of factors including the density, drag coefficient, attitude, and shape of the RSO. The satellites used for the HASDM calibration process are restricted by the requirement and assumption of a relatively constant BC. The model BC is estimated as part of an orbit determination process, and the true BC is the average of the model BCs over nearly 3200 orbits. The correction to the baseline density model is then estimated as the ratio of the model and true BC. This use of averaged BCs prohibits modeling of the small-scale spatial density variations.

In this paper, we develop a new approach to facilitate improved C_D estimates for RSOs toward collision avoidance, reentry prediction, and the possible use of debris objects that do not have relatively constant BCs for calibration of atmospheric models. The method uses light-curve measurements to estimate the attitude and rotational rates of RSOs with known shape models. The photometric observations used to estimate the RSO's attitude and angular rates can be collected from a variety of sources. The attitude and angular velocities are estimated using a nonlinear least-squares (NLSQ) estimator. This paper uses a NLSQ estimator [17] to solve the inverse problem of determining angular velocity and orientation given light-curve measurements. The NLSQ approach is one of the simplest inversion methods for solving nonlinear inverse problems. The nonlinear equations that model the RSO rotational dynamics and light-curve measurements are linearized and solved recursively [18].

The estimates from the NLSQ estimator are propagated forward in time and used to compute the C_D for the rocket body using a flat-plate panel method. We use a flat-plate panel method because of the simplified shape models used for the rocket bodies. Nearly all RSOs are in LEO at altitudes above ~200 km, where the atmosphere is free molecular i.e. atmospheric particles do not undergo intermolecular collisions. In free molecular flow, collisions between atmospheric particles are so infrequent that they can be neglected. Under such conditions, closed-form solutions for the C_D are available for simple convex RSO geometries such as a sphere, flat plate, and cylinder [19,20]. Closed-form solutions only exist for convex geometries because the concave geometries allow multiple reflections from the surface of the RSO and break a fundamental assumption of the solution that the incident velocity distribution function is Maxwellian. Simulations using computational methods, such as direct-simulation Monte Carlo, produce accurate estimates for the C_D but are computationally expensive, and therefore modeling the C_D becomes necessary [21,22].

The closed-form solution for the C_D of a flat plate with a single side exposed to the flow is especially useful because any arbitrary geometry (convex or concave) can be decomposed into small flat-plate panel elements. The total C_D for an arbitrary geometry is then approximated as the sum of the C_D of each of the flat-plate elements. For convex geometries, the approximation converges to the true C_D as the size of the flat-plate elements go to zero. For concave geometries, the approximation does not account for multiple reflections and flow shadowing and is generally in error by a few percent.

The developed methodology has the potential to substantially reduce orbit and reentry prediction uncertainties and provide extensive spatial and temporal coverage of density data sources without the need for launching expensive satellites. The organization of this paper is as follows. Section II provides the shape-model definition followed by Sec. III, which describes the light-reflection model for calculation of photon flux captured by a sensor. The following Sec. IV describes the NLSQ method, followed by Sec. V that describes the flat-panel method used to compute the C_D. Section VI presents and provides a discussion of the results, followed by conclusions and recommendations for future work.

II. Shape-Model Definition

The shape model considered in this paper consists of a finite number of flat facets, in which each facet has a set of basis vectors with which it is associated. Figure 1 shows a simple example of a spherical shape

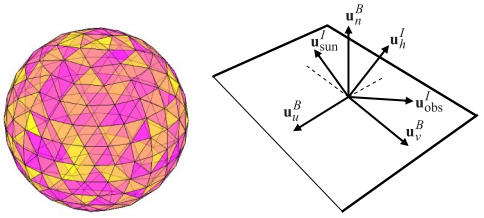

a) Shape model **b) Reflection geometry**

Fig. 1 Space object shape model and reflection geometry.

model along with the definition of the basis vectors that consist of three unit vectors $\boldsymbol{u}_n^B, \boldsymbol{u}_u^B$, and $\boldsymbol{u}_v^B$. The unit vector $\boldsymbol{u}_n^B$ points in the direction of the outward normal to the facet. For convex surfaces, this model becomes more accurate as the number of facets is increased. The vectors $\boldsymbol{u}_u^B$ and $\boldsymbol{u}_v^B$ are in the plane of the facet. The RSOs are assumed to be rigid bodies, and therefore the unit vectors $\boldsymbol{u}_n^B, \boldsymbol{u}_u^B$, and $\boldsymbol{u}_v^B$ do not change since they are expressed in the body frame.

The light-curve and the solar-radiation-pressure (SRP) models discussed in the next sections require that these vectors be expressed in inertial coordinates, and since the RSO body is rotating, these vectors will change with respect to the inertial frame. The body vectors can be rotated to the inertial frame by the standard attitude mapping given by

$$\boldsymbol{u}_k^B = A(\boldsymbol{q}_I^B)\boldsymbol{u}_k^I, \qquad k = n, u, v \tag{2}$$

where $A(\boldsymbol{q}_I^B)$ is the attitude matrix mapping the inertial frame to the body frame using the quaternion parameterization. Furthermore, the unit vector $\boldsymbol{u}_{\text{sun}}^I$ points from the RSO to the sun direction, and the unit vector $\boldsymbol{u}_{\text{obs}}^I$ points from the RSO to the observer. The vector $\boldsymbol{u}_h^I$ is the normalized half-vector between $\boldsymbol{u}_{\text{sun}}^I$ and $\boldsymbol{u}_{\text{obs}}^I$. This vector is also known as the sun–RSO–observer bisector. Each facet i has an area $\mathcal{A}_i$ with which it is associated. Once the number of facets has been defined and their basis vectors are known, the areas $\mathcal{A}_i$ define the size and shape of the RSO. To determine the SRP forces and light-curve characteristics, the surface properties must be defined for each facet.

The shape model used for this paper uses triangular facets defined by the location of their vertices $\boldsymbol{b}_i$ with respect to the center of mass of the object. Then, the area of the ith triangular facet is given by $\mathcal{A}_i = (1/2)\|\boldsymbol{d}_i \times \boldsymbol{l}_i\|$, where $\boldsymbol{d}_i$ and $\boldsymbol{l}_i$ are the vectors defining two sides of the facets or $\boldsymbol{d}_i = \boldsymbol{b}_{i,\text{v}_1} - \boldsymbol{b}_{i,\text{v}_2}$ and $\boldsymbol{l}_i = \boldsymbol{b}_{i,\text{v}_1} - \boldsymbol{b}_{i,\text{v}_3}$. The three vertices of the ith triangular facet are represented by v_1, v_2, and v_3. The unit normal vector is given by

$$\boldsymbol{u}_n^B(i) = \frac{\boldsymbol{d}_i \times \boldsymbol{l}_i}{\|\boldsymbol{d}_i \times \boldsymbol{l}_i\|} \tag{3}$$

III. Ashikhmin–Shirley Model

The optical sensor at the observing site records, in addition to the azimuth and elevation angles, the magnitude of the brightness of the RSOs. The observed brightness is a function of the manner in which light is reflected off the surface of the object. The two most common models used for reflection of light are diffuse, in which the light is scattered equally in all directions (Lambertian), and specular, in which the reflected light is concentrated about some direction (mirrorlike).

The brightness of an object in space can also be modeled using an anisotropic Phong light diffusion model or the Ashikhmin–Shirley (AS) model [23], which is based on the bidirectional reflectance distribution function (BRDF). We choose to use the AS BRDF model, among many that exist, because it has been known to provide fairly realistic light-curve reproduction [24]. There are multiple BRDF functions. The BRDF models the light distribution scattered from the surface due to the incident light and at any point on the surface as a function of two directions, the direction from which the light source originates and the direction from which the scattered light leaves the observed surface. The model in [23] decomposes the BRDF into a specular β_{spec} and a diffuse β_{diff} component. The two terms sum to give the total BRDF:

$$\beta_{\text{total}} = \beta_{\text{spec}} + \beta_{\text{diff}} \tag{4}$$

Reference [23] develops a model for continuous arbitrary surfaces but simplifies for flat surfaces. This simplified model is employed in this paper as shape models are considered to consist of a finite number of flat facets [23]. Therefore, the total observed brightness of an object becomes the sum of the contribution from each facet. Under the flat facet assumption, the specular term of the BRDF for the ith facet becomes [23]

$$\beta_{\text{spec}}(i) = \frac{\sqrt{[n_u(i)+1][n_v(i)+1]}}{8\pi} \times \frac{[\boldsymbol{u}_n^I(i)\cdot\boldsymbol{u}_h^I]^\eta}{\boldsymbol{u}_n^I(i)\cdot\boldsymbol{u}_{\text{sun}}^I + \boldsymbol{u}_n^I(i)\cdot\boldsymbol{u}_{\text{obs}}^I - [\boldsymbol{u}_n^I(i)\cdot\boldsymbol{u}_{\text{sun}}^I][\boldsymbol{u}_n^I(i)\cdot\boldsymbol{u}_{\text{obs}}^I]} F_{\text{reflect}}(i) \tag{5}$$

where the exponent η is given by

$$\eta = \frac{n_u(i)[\boldsymbol{u}_h^I\cdot\boldsymbol{u}_u^I(i)]^2 + n_v(i)[\boldsymbol{u}_h^I\cdot\boldsymbol{u}_v^I(i)]^2}{\{1-[\boldsymbol{u}_h^I\cdot\boldsymbol{u}_n^I(i)]^2\}} \tag{6}$$

with the Fresnel reflectance given as

$$F_{\text{reflect}}(i) = R_{\text{spec}}(i) + \Big[1 - R_{\text{spec}}(i)\Big]\Big[1 - \boldsymbol{u}_{\text{sun}}^I\cdot\boldsymbol{u}_h^I\Big]^5 \tag{7}$$

where R_{spec} is the specular reflectance coefficient. The parameters of the Phong model that dictate the directional (locally horizontal or vertical) distribution of the specular terms are n_u and n_v.

The terms in Eq. (5) are functions of the reflection geometry, which is described in Fig. 1. The diffuse term of the BRDF is given as

$$\beta_{\text{diff}}(i) = \left(\frac{28R_{\text{diff}}(i)}{23\pi}\right)\Big[1 - R_{\text{spec}}(i)\Big]\left[1 - \left(1 - \frac{\boldsymbol{u}_n^I(i)\cdot\boldsymbol{u}_{\text{sun}}^I}{2}\right)^5\right] \times \left[1 - \left(1 - \frac{\boldsymbol{u}_n^I(i)\cdot\boldsymbol{u}_{\text{obs}}^I}{2}\right)^5\right] \tag{8}$$

where $R_{\text{diff}}(i)$ is the diffuse coefficient for the ith facet. The model discussed previously assumes only single scattering and no self-shadowing.

For this paper, we assume that each facet has the same material parameters (specular coefficients, diffuse coefficients, and other reflection parameters discussed in the next section). We used $R_{\text{spec}} = R_{\text{diff}} = 0.5$ and $n_u = n_v = 10$. In practice, these values must be based on the known properties of the rocket body.

The apparent magnitude of an RSO is the result of sunlight reflecting off its surfaces along the line of sight to an observer. The fraction of visible sunlight that strikes an object (and is not absorbed) is computed as

$$F_{\text{sun}}(i) = \mathcal{C}_{\text{sun,vis}}\Big[\boldsymbol{u}_n^I(i)\cdot\boldsymbol{u}_{\text{sun}}^I\Big] \tag{9}$$

where $\mathcal{C}_{\text{sun,vis}} = 1062\ \text{W/m}^2$ is the power per square meter impinging on a given object due to visible light striking the surface. If for a facet either the angle between the surface normal and the observer's direction or the angle between the surface normal and sun direction is greater than $\pi/2$, there is no light reflected toward the observer from the facet, and the fraction of visible light for that facet is set to $F_{\text{sun}}(i) = 0$.

The fraction of sunlight reflected off a facet is then computed as

$$F_{\text{obs}}(i) = \frac{F_{\text{sun}}(i)\beta_{\text{total}}(i)\mathcal{A}(i)[\boldsymbol{u}_n^I(i)\cdot\boldsymbol{u}_{\text{obs}}^I]}{\|\boldsymbol{d}^I\|^2} \tag{10}$$

The light reflected off each facet is then used to compute the total photon flux measured by an observer as

$$F = \left[\sum_{i=1}^{N} F_{\text{obs}}(i)\right] \tag{11}$$

The total photon flux is then used to compute the apparent brightness magnitude as

$$\tilde{m}_{\text{app}} = -26.7\text{–}2.5\log_{10}\left|\frac{F}{C_{\text{sun,vis}}}\right| + v_{\text{sensor}} \tag{12}$$

where v_{sensor} is the measurement noise associated with the apparent magnitude and -26.7 is the apparent magnitude of the sun [2]. We assume a zero-mean white-noise process with a standard deviation σ for v_{sensor}.

IV. Nonlinear Least Squares

The estimation approach chosen for this paper is the NLSQ method. This method is a batch method and therefore processes all the data at once. To apply the NLSQ method to attitude and angular velocity determination, one must linearize both the measurement and dynamic models. Also, the attitude representation chosen for this paper is the quaternion, and therefore the attitude error must be approximated by a small angle error to avoid the quaternion unit constraint [18]. The goal is to estimate a state $\boldsymbol{x}_k = [\,\boldsymbol{q}^T(t_k) \quad \boldsymbol{\omega}_r^T(t_k)\,]^T$ (composed of the full quaternion and the three angular velocity components) for times t_k from measurements $\tilde{z}_k$ for $k = 1, \ldots, p$, where p is the number of measurements.

Consider the dynamic and measurement models, assuming measurements with uncorrelated measurement errors,

$$\boldsymbol{x}_{k+1} = \boldsymbol{f}_k(\boldsymbol{x}_k) \tag{13a}$$

$$\tilde{z}_k = \boldsymbol{g}_k(\boldsymbol{x}_k) + \boldsymbol{n}_k \tag{13b}$$

where $\boldsymbol{n}_k \sim \mathcal{N}(\boldsymbol{n}_k; 0, \Sigma_k^2)$ and $E\{\boldsymbol{n}_k\boldsymbol{n}_j\} = \delta_{kj}\Sigma_k^2$ with δ_{kj} being the Kronecker delta function. We assume no process noise, but it can be added when processing real data to account for unmodeled or mismodeled dynamics. Equations (13a) and (13b) can then be used to estimate the initial condition of the system $\boldsymbol{x}_o$ by writing the measurements as $\tilde{z}_k = \boldsymbol{g}_k[\boldsymbol{\phi}_k(\boldsymbol{x}_o)] + \boldsymbol{n}_k$ where $\boldsymbol{\phi}_k(\cdot)$ takes the initial conditions and maps them to time k. The measurements can be written in vector form as

$$\tilde{\boldsymbol{y}} = \boldsymbol{h}(\boldsymbol{x}_o) + \boldsymbol{v} \tag{14}$$

where $\tilde{\boldsymbol{y}} = [\tilde{z}_1^T, \ldots, \tilde{z}_p^T]^T$, $\boldsymbol{v} \sim \mathcal{N}(\boldsymbol{v}; 0, R)$, $R = \text{diag}(\Sigma_1^2, \ldots, \Sigma_p^2)$, and $\boldsymbol{h}(\cdot) = \boldsymbol{g}_k(\boldsymbol{\phi}_k(\cdot))$. In the previous and following equations, the $\sim$ overhead accent signifies measured values, whereas the $\hat{}$ overhead accent signifies predicted values. The system in Eq. (13) can be solved using the NLSQ method by linearizing the system about the current estimate. Using a Taylor series expansion, the measurement function from Eq. (14) can be written as

$$\boldsymbol{h}(\boldsymbol{x}_o) = \boldsymbol{h}(\hat{\boldsymbol{x}}_o) + H(\hat{\boldsymbol{x}}_o)(\hat{\boldsymbol{x}}_o - \boldsymbol{x}_o) + \mathcal{O}(2) \tag{15}$$

where $\mathcal{O}(2)$ is neglected higher-order terms and H is given as

$$H_k^i = \frac{\partial \boldsymbol{g}_k(\boldsymbol{x}_k)}{\partial \boldsymbol{x}_k}\frac{\partial \boldsymbol{\phi}_k(\boldsymbol{x}_o)}{\partial \boldsymbol{x}_o}\bigg|_{x_o=\hat{x}_o^i} = \frac{\partial \boldsymbol{g}_k(\boldsymbol{x}_k)}{\partial \boldsymbol{x}_k}\boldsymbol{\Phi}(t_k, t_0) \tag{16}$$

where $\hat{\boldsymbol{x}}_o^i$ is the estimate for the ith iteration, $H^i = [H_1^i, \ldots, H_p^i]^T$, and $\boldsymbol{\Phi}(t_k, t_o)$ is the state transition matrix about the estimated trajectory calculated as shown in the Appendix. The derivatives of the measurement function $\boldsymbol{g}_k(\cdot)$ and the dynamic function $\boldsymbol{\phi}_k(\cdot)$ must be calculated. The derivatives of $\boldsymbol{g}_k(\cdot)$ can be derived from the equations in Sec. III and are given in [23]. The derivatives of $\boldsymbol{\phi}_k(\cdot)$ involve the linearization of attitude kinematics and dynamic equations and are shown later in the Appendix.

The NLSQ solution is obtained by minimizing the following cost function [18]:

$$L(\hat{\boldsymbol{x}}_o) = \frac{1}{2}\Big[\tilde{\boldsymbol{y}} - \boldsymbol{h}(\hat{\boldsymbol{x}}_o)\Big]^T R^{-1}\Big[\tilde{\boldsymbol{y}} - \boldsymbol{h}(\hat{\boldsymbol{x}}_o)\Big] \tag{17}$$

Note that the minimization problem in Eq. (17) is a constrained one and is usually solved using unconstrained local attitude parameterization [25]. Therefore, this paper uses two attitude representations, a local error attitude and a global attitude parameter, which use the quaternion $\boldsymbol{q}$ and the small Euler angle $\delta\xi$, respectively. The state vector for the local error attitude is given by $\boldsymbol{x}_{o,r} = [\,\delta\xi^T \quad \boldsymbol{\omega}_r^T\,]^T$. The formal NLSQ iterative solution using the local error attitude can then be written as

$$\hat{\boldsymbol{x}}_{o,r}^{i+1} = \hat{\boldsymbol{x}}_{o,r}^i + \Big[H^{iT}R^{-1}H^i\Big]^{-1}H^{iT}R^{-1}\Big[\tilde{\boldsymbol{y}} - \boldsymbol{h}(\hat{\boldsymbol{x}}_o^i)\Big] \tag{18}$$

where $\hat{\boldsymbol{x}}^i_{o,r} = [\,(\delta\hat{\boldsymbol{\xi}}^i)^T \quad (\hat{\boldsymbol{\omega}}^i_r)^T\,]^T$ with

$$P^i_o = E\left\{(\hat{\boldsymbol{x}}^i_{o,r} - \boldsymbol{x}_{o,r})(\hat{\boldsymbol{x}}^i_{o,r} - \boldsymbol{x}_{o,r})^T\right\} \quad \text{and} \quad P^i_o = (H^{i^T} R^{-1} H^i)^{-1} \tag{19}$$

and where the predicted covariance for the residuals is calculated as

$$P^i_{yy} \equiv E\left\{(\hat{\boldsymbol{y}}^i - \tilde{\boldsymbol{y}})(\hat{\boldsymbol{y}}^i - \tilde{\boldsymbol{y}})^T\right\} = H^{i^T} P^i_o H^i + R \quad \text{and} \quad \hat{\boldsymbol{y}}^i = \boldsymbol{h}(\hat{\boldsymbol{x}}^i_o) \tag{20}$$

Equation (19) gives the predicted state at the current iteration in the Euler angle $\boldsymbol{\xi}$ space, which under the small angle assumption can be converted to the quaternion $\boldsymbol{q}$ space as

$$\hat{\boldsymbol{q}}^{i+1} = \hat{\boldsymbol{q}}^i + \frac{1}{2}\Xi(\hat{\boldsymbol{q}}^i)\delta\hat{\boldsymbol{\xi}}^{i+1} \tag{21}$$

where $\delta\hat{\boldsymbol{\xi}}^{i+1}$ is set to zero after each iteration and $\Xi(\cdot)$ is defined in the Appendix. The state vector using the global attitude parameter is given by $\hat{\boldsymbol{x}}^{i+1}_o = [\,\hat{\boldsymbol{q}}^{i+1T} \quad \hat{\boldsymbol{\omega}}^T_r\,]^T$. The estimate of $\hat{\boldsymbol{x}}_{o,r}$ is obtained using Eq. (18) iteratively until a termination condition is met. We provide the solver with two conditions, the maximum number of iterations $i_{\max}$ and the relative tolerance computed as

$$\epsilon = \frac{\|\hat{\boldsymbol{x}}^{i+1}_{o,r} - \hat{\boldsymbol{x}}^i_{o,r}\|}{\|\hat{\boldsymbol{x}}^i_{o,r}\|} \tag{22}$$

We use a residual tolerance of $\epsilon = 1 \times 10^{-15}$ (the tolerance is not optimized, and a larger value may be used) and set the maximum number of iterations at $i_{\max} = 200$ for this paper. The solution allows for a covariance to be computed for each time step by using P_o and the linearized dynamic equations, which in turn can be used to represent uncertainty in C_D that is computed from the orientation estimates.

The NLSQ algorithm requires the user to provide an initial guess for the state of the system. The NLSQ estimator can be sensitive to the accuracy of the initial state, resulting in either divergence or convergence onto a local minima that is different from the true solution. Converging onto the true solution may require the data to be processed multiple times through the NLSQ algorithm. The approach used for initializing the NLSQ algorithm is discussed in Sec. VI.

V. Flat-Plate Panel Method

The attitude estimate from the NLSQ estimtor is propagated forward in time with the orbit and used to compute $\mathcal{C}_D$ when the RSO altitude is below 1000 km. The pressure and shear contribution of each facet in the free molecular flow is computed using the closed-form solution of Schaaf and Chambre [19]. The pressure $\mathcal{C}_P$ and shear $\mathcal{C}_\tau$ solutions as functions of the local flow inclination angle θ for a flat plate with a single side exposed to the flow and quasi-specular reflection are given in Eqs. (23) and (24), respectively. The local inclination angle is defined as $\theta_i = \arccos(-\boldsymbol{v}_{\text{rel}} \cdot \boldsymbol{u}^B_{n_i})$, where $\boldsymbol{u}^B_n$ is the facet normal unit vector in the body frame and i represents the ith facet,

$$\mathcal{C}_{P_i} = \frac{1}{s^2}\left[\left(\frac{2-\sigma_n}{\sqrt{\pi}} s\cos\theta_i + \frac{\sigma_n}{2}\sqrt{\frac{T_w}{T_\infty}}\right)e^{-(s\cos\theta_i)^2} + \left\{(2-\sigma_n)\left[(s\cos\theta_i)^2 + \frac{1}{2}\right] + \frac{\sigma_n}{2}\sqrt{\frac{\pi T_w}{T_\infty}} s\cos\theta_i\right\}\left[1 + \operatorname{erf}(s\cos\theta_i)\right]\right] \tag{23}$$

$$\mathcal{C}_{\tau_i} = -\frac{\sigma_t \sin\theta_i}{s\sqrt{\pi}}\left[e^{-(s\cos\theta_i)^2} + \sqrt{\pi} s \sin\theta_i (1 + \operatorname{erf}(s\cos\theta_i))\right] \tag{24}$$

Here, σ_n and σ_t are the normal and tangential momentum accommodation coefficients, respectively; T_w is the object wall temperature; T_∞ is the atmospheric temperature; and s is the speed ratio defined by

$$s = \frac{|\boldsymbol{v}_{\text{rel}}|}{v_{\text{mp}}} \tag{25}$$

where v_{mp} is the most probable speed of a Maxwellian velocity distribution at the local translational temperature of the atmosphere T_∞ and is defined by

$$v_{\text{mp}} = \sqrt{\frac{2k_B T_\infty}{m_p}} \tag{26}$$

Here, k_B is the Boltzmann constant, and m_p is the atmospheric particle mass. The error function $\operatorname{erf}(x)$ is defined as

$$\operatorname{erf}(x) = \frac{2}{\sqrt{\pi}}\int_0^x e^{-t^2}\,\mathrm{d}t \tag{27}$$

The differential force coefficient $\boldsymbol{C}_f$ due to a triangular element can then be calculated as (we use a formulation similar to that in [26])

$$d\boldsymbol{C}_{fi} = \left(C_{P_i}\boldsymbol{u}^B_{n_i} + C_{\tau_i}\boldsymbol{u}^B_{t_i}\right)\mathcal{A}_i \tag{28}$$

where $\boldsymbol{u}^B_t$ is the unit tangential vector in the body frame. The tangential vector lies in the plane of the facet in a direction opposite to the local flow direction. The normalized tangential vector is calculated by subtracting the unit velocity vector from the isolated normal component as

$$\boldsymbol{u}^B_t = \frac{\boldsymbol{u}^B_n(\boldsymbol{u}^B_{v_{\text{rel}}} \cdot \boldsymbol{u}^B_n) - \boldsymbol{u}^B_{v_{\text{rel}}}}{\sqrt{1 - (\boldsymbol{u}^B_{v_{\text{rel}}} \cdot \boldsymbol{u}^B_n)^2}} \tag{29}$$

where $\boldsymbol{u}^B_{v_{\text{rel}}}$ is the unit velocity vector. Assigning the object a conventional flight dynamics body axis allows us to define $\boldsymbol{u}_{v_{\text{rel}}}$ in terms of body orientation angles γ (pitch) and ψ (yaw) as

$$\boldsymbol{u}_{v_{\text{rel}}} = [\,\cos\gamma\cos\psi \quad -\cos\gamma\sin\psi \quad \sin\gamma\,] \tag{30}$$

The total force coefficients along the body axes (axial A, side S, and normal N) can then be calculated as the integral of the differential force coefficients over the entire body as

$$\begin{bmatrix}\mathcal{C}_A\\ \mathcal{C}_S\\ \mathcal{C}_N\end{bmatrix} = \frac{1}{\mathcal{A}_{\text{ref}}}\iint_S \mathrm{d}\boldsymbol{C}_{fi} \tag{31}$$

where N is the number of facets making up the body and $\mathcal{A}_{\text{ref}}$ is the reference projected area calculated as

$$\mathcal{A}_{\text{ref}} = \sum_{i=1}^{N} \mathcal{A}_i \cos(\theta_i)\zeta \tag{32}$$

where $\zeta = 1$ for $\text{abs}(\theta_i) \le 90$ deg and $\zeta = 0$ otherwise. The $\mathcal{C}_D$ for the object can then be calculated using the body axis force coefficients in conjunction with the body orientation angles as

$$\mathcal{C}_D = \begin{bmatrix}\mathcal{C}_A\\ \mathcal{C}_S\\ \mathcal{C}_N\end{bmatrix}^T \cdot \begin{bmatrix}\cos\gamma\cos\psi\\ -\cos\gamma\sin\psi\\ \sin\gamma\end{bmatrix} \tag{33}$$

A. Surface Contamination

The momentum and energy exchange that characterizes the physical $\mathcal{C}_D$ is influenced by the adsorption of atomic oxygen that may partially or completely cover the surface of a RSO in LEO. The atmospheric particles interacting with a clean surface are assumed to

be specularly reflected, while those that interact with the atomic oxygen covering the surface are assumed to reflect diffusely after surrendering a finite amount of its incoming energy.

The energy accommodation coefficient has been recently modeled as a function of the partial pressure of atomic oxygen using a Langmuir adsorption isotherm and is described as [27]

$$C_D = (1 - \Theta)C_{D,s} + \Theta C_{D,\text{ads}} \tag{34}$$

where $C_{D,s}$ is the drag coefficient based on a clean surface, $C_{D,\text{ads}}$ is the drag coefficient based on a surface completely covered with an adsorbate (atomic oxygen), and Θ is the fraction of surface coverage. $C_{D,s}$ and $C_{D,\text{ads}}$ are computed separately using Eqs. (23–33) as described previously, in which the total energy accommodation coefficient for the adsorbate is assumed to be unity and that for a clean surface is calculated using Goodman's formula [28] as

$$\alpha_s = \frac{K_s \mu}{(1 + \mu)^2} \tag{35}$$

where the value of K_s can lie between 2.4 and 3.6 depending on the shape of the RSO. In this paper, we use a value of 3.0 for the rocket bodies [21].

Furthermore, in the quasi-specular Cercignani–Lampis–Lord (CLL) [29] model used in this paper, the total energy accommodation coefficient is the average of the normal α_n and tangential α_t energy accommodation coefficients:

$$\alpha = \frac{\alpha_n + \alpha_t}{2} \tag{36}$$

In the CLL model, α_t is unity when σ_t is unity. Therefore, Eq. (36) can be rewritten as

$$\alpha_n = 2\alpha - 1 \tag{37}$$

Goodman's model for the energy accommodation of a clean surface is combined with Eq. (37) to find the normal energy accommodation coefficient for the surface as

$$\alpha_n = 2\frac{K_s \mu}{(1 + \mu)^2} - 1 \tag{38}$$

The normal energy accommodation coefficient α_n is used to calculate the normal momentum accommodation σ_n using the following relation [27], which can be plugged into Eq. (23). An extensive literature search reveals that σ_t is unity for free molecular flow, which is plugged into Eq. (24) [30–32],

$$\sigma_n = 1 - \sqrt{1 - \alpha_n} \tag{39}$$

The surface coverage Θ in Eq. (34) is modeled using the Langmuir isotherm

$$\Theta = \frac{K_L P_O}{1 + K_L P_O} \tag{40}$$

where K_L is the Langmuir fitting constant and P_O is the partial pressure of atomic oxygen [27]. Models for use with both the diffuse and quasi-specular reflection kernels have been developed in [27].

B. Mixture of Gases

The atmosphere in LEO is comprised of a mixture of gases. For computing the C_D in LEO, six different neutral species are typically accounted for, and this paper uses the same [21,22,27,33]. When computing the C_D for a mixture of gases, the total C_D is the sum of the individual species C_D weighted by the species mole fraction and particle mass and normalized by the average mass of the mixture m_{avg}:

$$C_{D,T} = \frac{1}{m_{\text{avg}}} \sum_{j=1}^{M} \chi_j m_j C_{D,j} \tag{41}$$

NRLMSISE-00 is used to compute the mole fractions χ_j for each species. Here, M is the total number of species, and m_{avg} is computed from

$$m_{\text{avg}} = \sum_{j=1}^{M} \chi_j m_j \tag{42}$$

Finally, the overall C_D is computed as follows:

$$C_{D,\text{overall}} = (1 - \Theta) \sum_{j=1}^{M} C_{D,T(s)} + \Theta \sum_{j=1}^{M} C_{D,T(\text{ads})} \tag{43}$$

VI. Results

This section describes the setup and discusses results for the simulation cases using the proposed method. We consider four different shape models as shown in Fig. 2. The shape models used are a cylinder with round top (Fig. 2a), a cylinder (Fig. 2b), an Atlas upper stage (Fig. 2c), and a Falcon 9 upper stage (Fig. 2d) model. Each model uses the same initial attitude and positions states and with the simulation conditions given in the following:

1) The geographic position of the ground site is 0° North, 0° West with 0 km altitude.

2) The orbital elements are given by $a = 25864.16932$ km, $e = 0.743$, inc $= 30.0083$ deg, $\omega = \Omega = 0.0$ deg, and $M_0 = 90.065$ deg.

3) The initial time of the simulation was 15 June, 2010, at 18:00.00 UTC (coordinated universal time).

4) An initial quaternion is

$$\boldsymbol{q}_I^B = \begin{bmatrix} 0.7041, & 0.0199, & 0.0896, & 0.7041 \end{bmatrix}^T$$

5) A constant rotation rate, defined as the body rate with respect to the inertial frame (represented in body coordinates), is used and is given by:

$$\boldsymbol{\omega}_{rB/I}^B = [0.200, 0.0180, 0.0524]^T \text{ rad/s}$$

The true quaternion and angular velocity are shown in Fig. 3 with all simulation cases having the same true orientational trajectories. The trajectories are derived using the Euler kinematic equations provided in the Appendix. For all the simulations, measurements of apparent magnitude are produced using zero-mean white-noise error processes with a standard deviation of 0.05 for magnitude. The time interval between the measurements is set to 0.5 s, and data are simulated for 120 s, which is a reasonable assumption for the collection of real data for the rotational rates used.

The initial guess for the state provided to the NLSQ algorithm for the simulation cases is sampled from a uniform distribution. The uniform distribution uses the true state as the mean with errors of 50 deg for all three attitudes and 1000 deg/h for the rotational rate. It is important to note that when processing real light-curve measurements larger errors can be used for the attitude, while the angular velocity distribution can be based on practical knowledge. The sampling strategy is shown in Fig. 4. The NLSQ estimator diverges if the sample falls outside the radius of convergence. Convergence is judged based on performance through minimization of the cost function given in Eq. (17). The convergence is also judged based on the measurement residuals and the z-score for the measurements computed as [34]

$$Z = \left(\hat{\boldsymbol{y}}^i - \tilde{\boldsymbol{y}}\right)^T P_{yy}^{i-1} \left(\hat{\boldsymbol{y}}^i - \tilde{\boldsymbol{y}}\right) \tag{44}$$

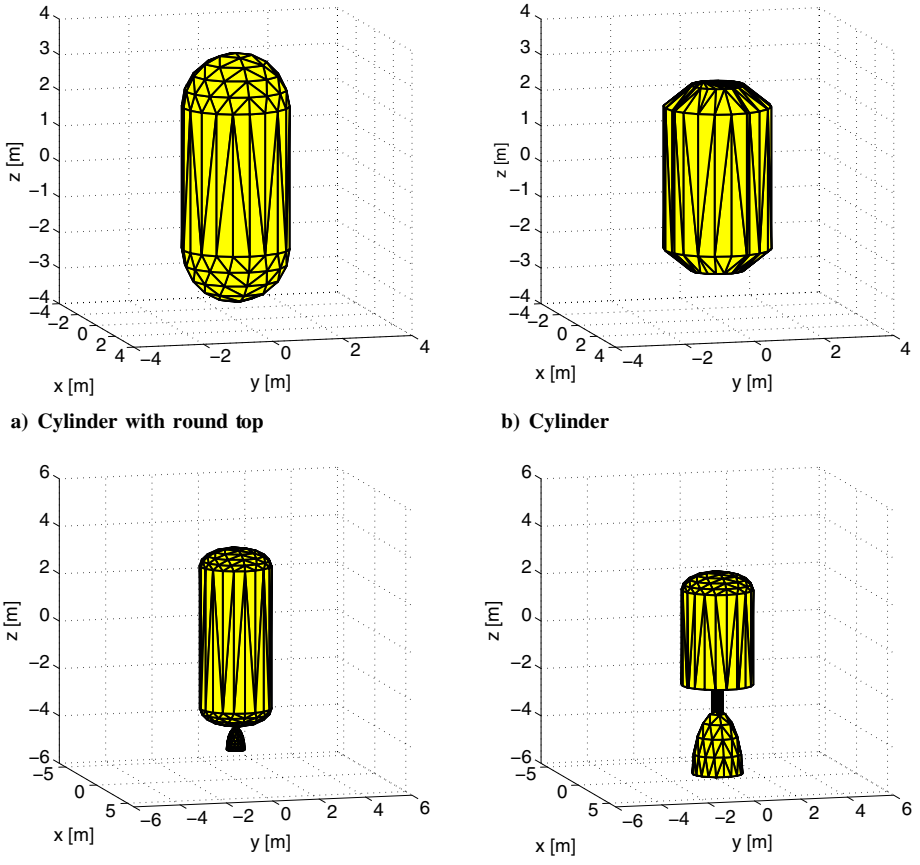

a) Cylinder with round top

b) Cylinder

c) Atlas upper stage

d) Falcon 9 upper stage

Fig. 2 Representative shape models for rocket bodies.

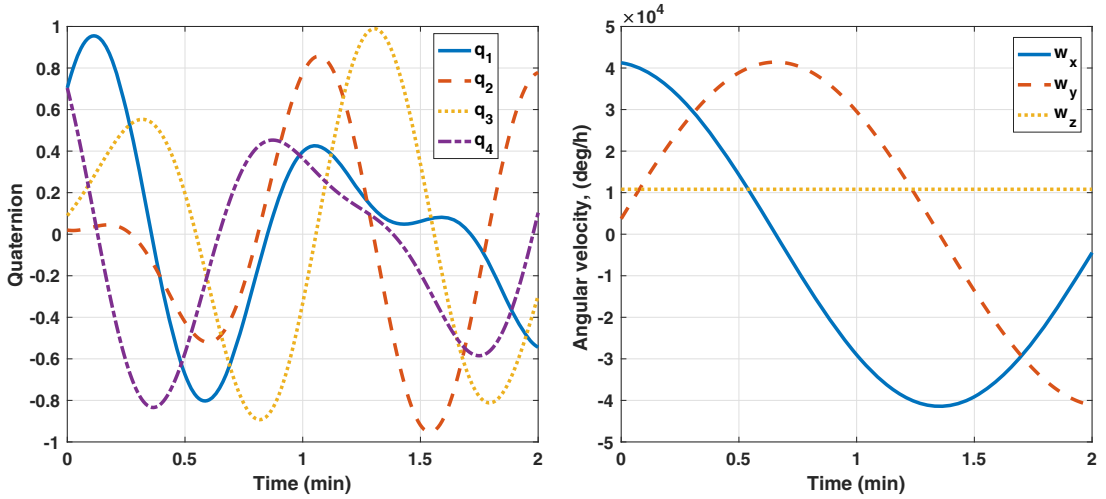

Fig. 3 True attitude and angular velocity profile.

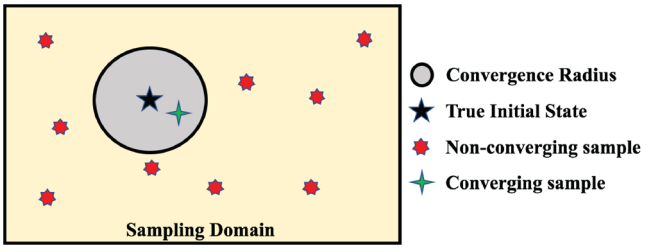

Fig. 4 Sampling for NLSQ initial-state guess.

The residual test is also used because in certain cases the NLSQ estimator converges but the estimated light curve does not have good residuals. The distribution is sampled until convergence is achieved.

Figures 5–8 show the magnitude measurements simulated using Eq. (12) and the estimated solution using the NLSQ algorithm for the cylinder with a round top, the cylinder, the Atlas, and the Falcon shape models, respectively. The light-curve profiles for the different geometry models can vary significantly depending on the initial state. In this instance, the light curves for all the shape models have similar overall profiles with differences arising due to the concave features of

the different shape models. For example, light curves for all shapes models have two peaks due to the smooth side (head) of the object. However, a third peak seems to be generated due to the concave features that starts small for the cylinder model but grows for the Atlas model that has a small nozzle to a large peak for the Falcon model that has a large nozzle. The round top model has no sharp or concave features in the geometry, and therefore the entire light curve is smooth and continuous. The third peak for the other three models with concave features becomes sharper with more complex features resulting in light curves with abruptly changing magnitudes. For all the shape models, the proposed approach shows good performance in terms of the measurement residual and by how well the predicted observations match the observations as shown in Figs. 5–8. The scale in the figures for the apparent magnitude or brightness of the RSO is reversed because a lower magnitude represents a brighter source; e.g., the apparent magnitude of the sun is −26.74.

The initial-state vector estimates from the NLSQ estimator for the four different shape models are given in Table 1. For all shape models, the NLSQ solution converges onto the true solution. It is possible, however, that the light curves for the models do not show the same observability in terms of the estimated attitude and angular velocity. The NLSQ approach can converge to local solutions that do not make

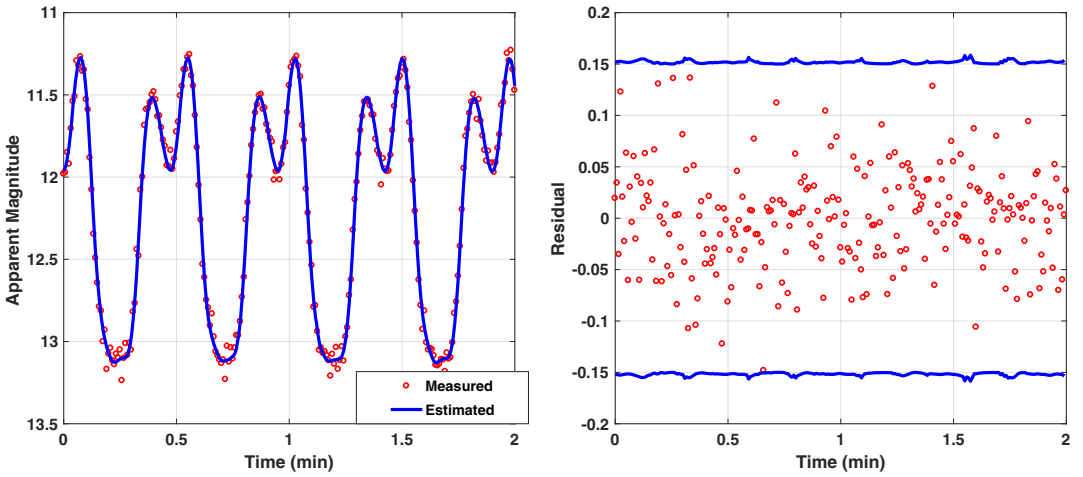

Fig. 5 NLSQ results for cylinder with round top rocket body model. Left: measured and estimated magnitude; right: residual.

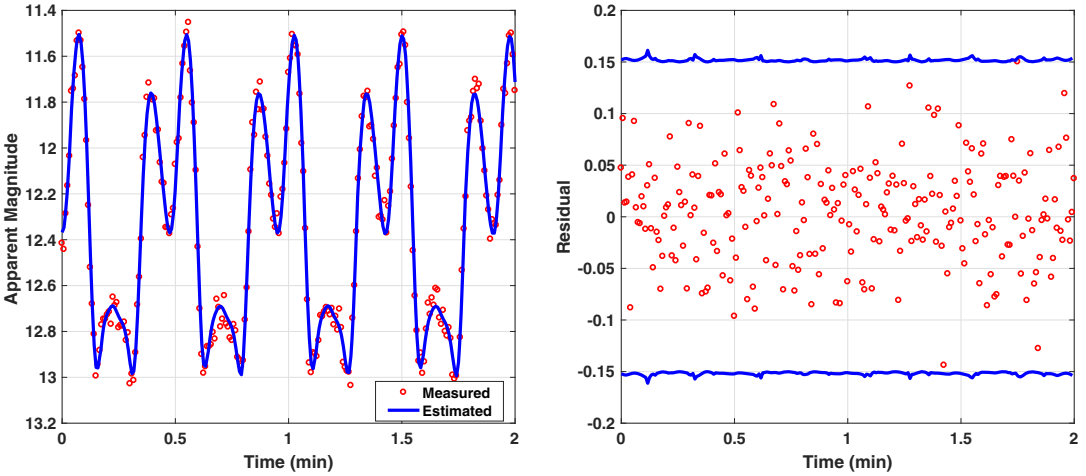

Fig. 6 NLSQ results for cylinder rocket body model. Left: measured and estimated magnitude; right: residual.

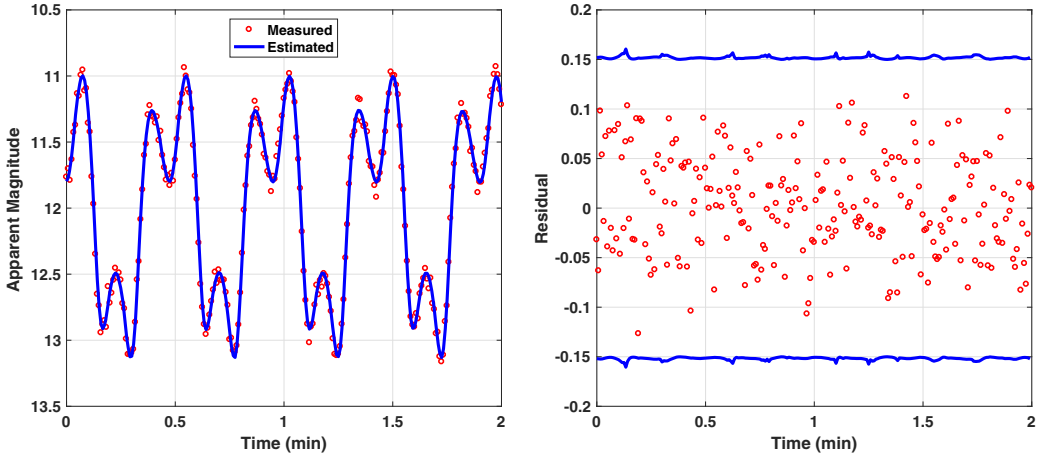

Fig. 7 NLSQ results for Atlas rocket body model. Left: measured and estimated magnitude; right: residual.

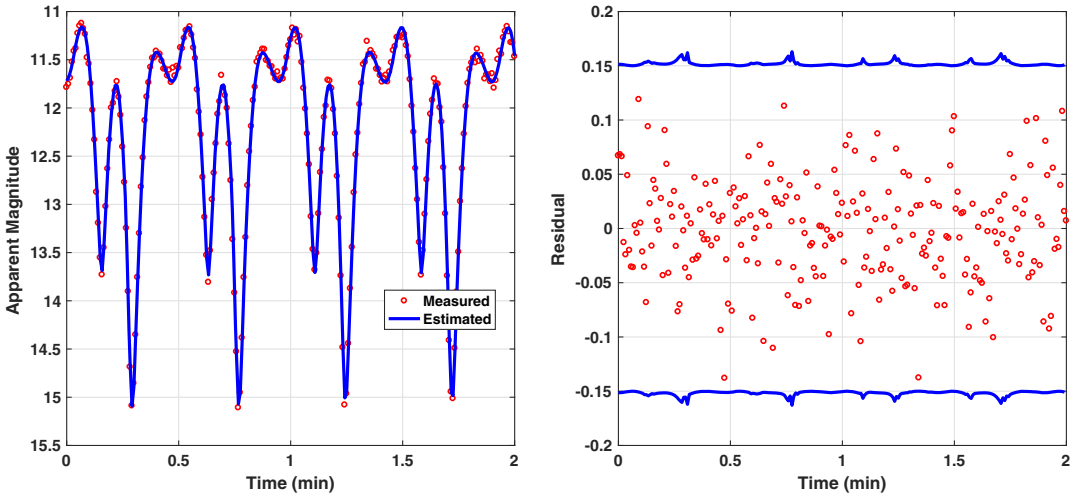

Fig. 8 NLSQ results for Falcon 9 rocket body model. Left: measured and estimated magnitude; right: residual.

the true rotational states very well but fit the observations. This is due to the fact that these shapes have symmetries and therefore have multiple possible solutions. A way around this could be to estimate just the axis of symmetry and not the full attitude. These ambiguities are briefly discussed in the following and will be studied more in future work, but the method can still predict the observations very well. It should also be noted that, because of the symmetries in the shape models, the convergence onto a local and not a true solution does not affect the calculations for C_D.

In this paper, we estimate the full quaternion because we develop the method for application to all objects (symmetric and nonsymmetric). In the results in Table 2, it is observed that the uncertainty in the initial state is the largest in the symmetry direction ξ_z. The full quaternion is observable in this paper because of the facets (meshing) that break the symmetry. In the limit where a large enough number of facets used maintains the symmetry, it is expected that this uncertainty will be very large, possibly infinity.

With this in mind, we modified our code to estimate only two observable attitude states. We ran a test case with Falcon, the results for which are also presented in Tables 1 and 2. It is seen that the estimator does well again with smaller uncertainties in the observable states. The angular velocity corresponding to the unobservable attitude state is nonzero because of the cross-coupling in the momentum, which makes the angular velocity observable.

Table 1 NLSQ estimates of the initial-state vector ((·) means that the value is not computed.)

					Falcon	
Parameter	True	Round top	Cylinder	Atlas	Three axis	Two axis
q_1	0.7041	0.7072	0.6955	0.7023	0.6956	0.6961
q_2	0.0199	0.0378	0.0352	0.0521	−0.0959	0.1106
q_3	0.0896	0.0698	0.0710	0.0560	0.2048	(·)
q_4	0.7041	0.7025	0.7141	0.7077	0.6819	0.7094
ω_{r_x}, rad/s	0.200	0.1985	0.1988	0.1976	0.1949	0.1889
ω_{r_y}, rad/s	0.0180	0.0271	0.0292	0.0369	−0.0483	0.0679
ω_{r_z}, rad/s	0.0524	0.0531	0.0524	0.0521	0.0525	0.0525

Table 2 Estimates of the NLSQ initial-state variance

				Falcon	
Parameter	Round top	Cylinder	Atlas	Three axis	Two axis
ξ_x, rad	0.0259	0.0205	0.0133	0.0031	0.0024
ξ_y, rad	0.0034	0.0031	0.0027	0.0021	0.0015
ξ_z, rad	0.0672	0.0610	0.0519	0.0315	(·)
ω_{r_x}, rad/s	0.0016	0.0016	0.0018	0.0016	0.00012
ω_{r_y}, rad/s	0.0135	0.0122	0.0101	0.0061	0.00020
ω_{r_z}, rad/s	0.0006	0.0005	0.0002	0.0001	0.00002

VII. Effect of Attitude on Orbit and Reentry Prediction

In the previous section, an approach for estimating the attitude and the corresponding rotational rates using the NLSQ estimator with light-curve data was presented. The method is shown to work well in estimating the attitude and its variations for the simulated cases. In this section, we present an analysis to characterize the importance of estimating the attitude on drag and orbit prediction. The estimates from the NLSQ solution given in Table 1 are propagated forward in time with the orbit and used to compute C_D using the equations from Sec. V. The C_D computed for the different shape models along their respective orbit at altitudes below 1000 km are shown in Fig. 9. The differences in the C_D shown are due to the shape models since all the models have the same rotational dynamics. It is assumed that there are no external torques acting on the rocket body. It is seen that the attitude can cause significant variations in the C_D for each of the rocket body shape models (by up to 50% between the minimum and maximum values for the Falcon rocket body). The uncertainty in C_D can be characterized using the solution from the NLSQ estimator and the associated variance given in Table 2. Sampling is performed on the NLSQ solution, and C_D are computed for each of these samples. Figure 10 shows the uncertainty in C_D due to the uncertainty in the NLSQ solution for the round top shape model. The uncertainty along the orbit is computed using unscented transformations [35] and validated with a Monte Carlo simulation using 1000 members. It is seen that the covariance for C_D does change along the trajectory and has different sensitivities at different altitudes. These values could be used directly for orbit propagation and orbit determination.

Figure 11a shows the comparison of C_D for a rotating and nonrotating Falcon rocket body model. It is seen from Fig. 11a that Falcon undergoes quick attitude variations with the C_D varying a significant amount of up to 50%. For completeness, we also use a constant value of C_D representative of using a constant fitted value of BCs. The constant C_D is computed as the mean of the C_D for the rotating case for a single pass below 1000 km. Similarly, a constant $\mathcal{A}$ is computed as the mean of the $\mathcal{A}$ for the rotating case. The mass for the models is assumed to be 1000 kg. The BCs computed for all the shape models are given in Table 3.

Figure 11b shows the error in orbit caused by not accounting for the attitude variations and using a constant BC. The orbit is propagated using the true initial state for quaternion and rotational rates, accounting for two-body dynamics, spherical harmonics up to order 6 (J1–J6), and atmospheric drag. Results show that, if not properly accounted for, the attitude variations can lead to a maximum orbit prediction error of more than 20 km after just ten brief passes through the lower atmosphere or 120 h. Using a fitted BC can result in an even larger maximum position error of about 35 km in the same amount of time. The error is zero until the first pass through the atmosphere and grows every orbit, peaking to a growing maximum value at perigee for each orbit. The position

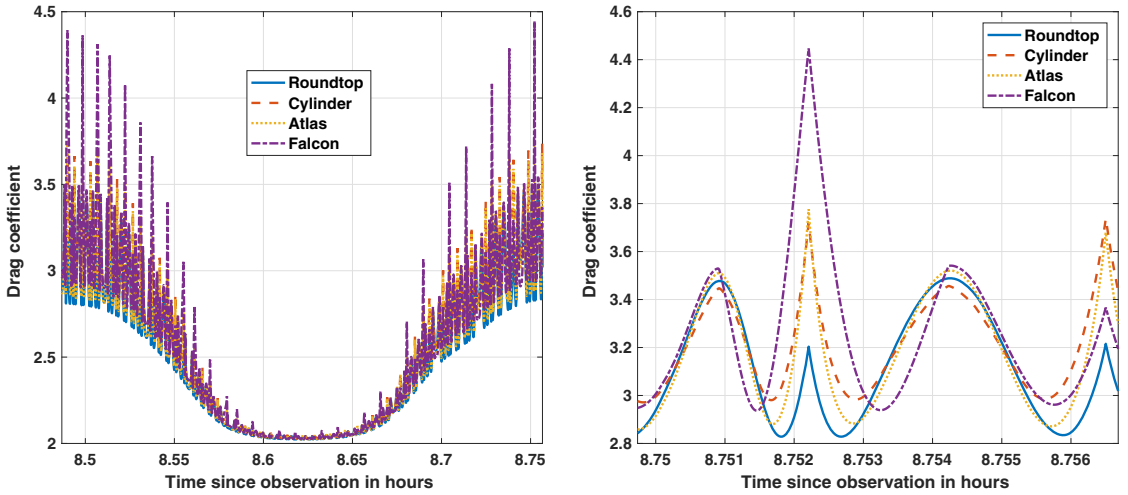

Fig. 9 Comparison of C_D for different shape models. Left: comparison of C_D below 1000 km; right: closeup of C_D variations.

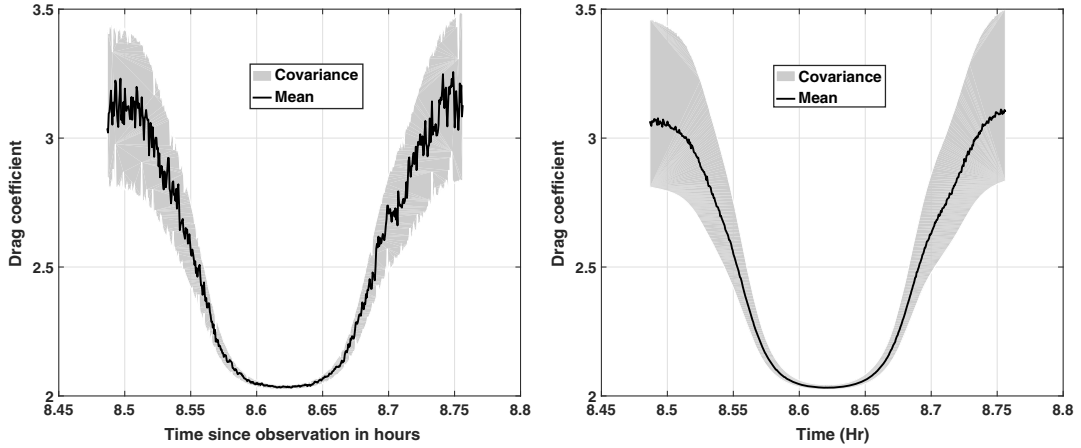

Fig. 10 Sampling for NLSQ initial-state guess. Left: propagation of sigma points; right: Monte Carlo.

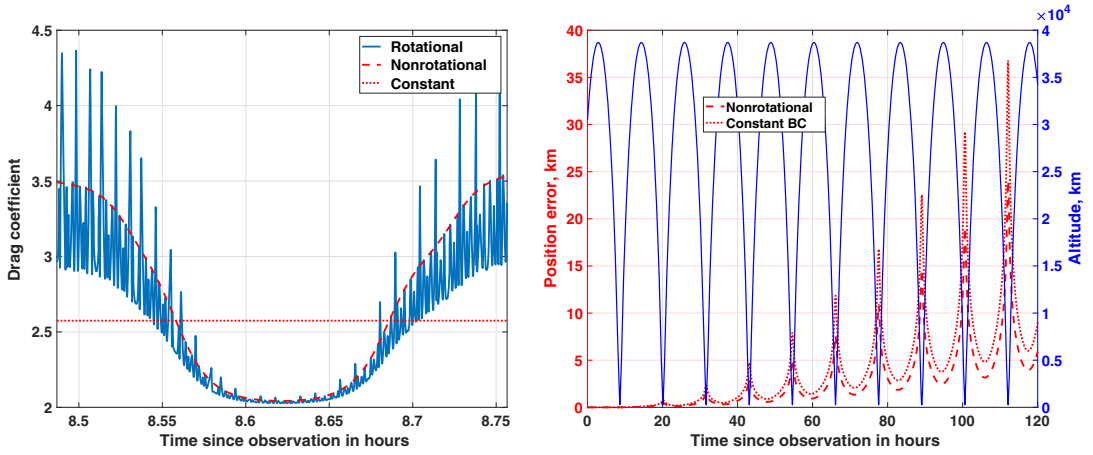

Fig. 11 Effect of attitude on orbit prediction for Falcon. Left: C_D below 1000 km; right: position error.

errors are computed as the magnitude of the difference in the position vectors at the same time along the orbits with respect to the rotating case.

Table 3 Estimates of ballistic coefficients for the different shape models

Parameter	Round top	Cylinder	Atlas	Falcon
Mean C_D	2.498	2.555	2.531	2.577
Mean A, m^2	18.953	14.703	22.020	16.826
BC, m^2/kg	0.0473	0.0376	0.0557	0.0434

Figure 12 shows the comparison of orbit errors for all the different shape models. It is seen that for all shape models the errors for the case of a constant BC are significantly higher than that of a nonrotating RSO. In both cases, the errors are largest for the Atlas among all shape models due to the largest BC as given in Table 3. The maximum error for Atlas using a constant BC can reach upward of 100 km after just ten orbits and upward of 60 km for the nonrotating scenario. The round top, Falcon, and cylinder models show errors in the decreasing order behind the Atlas model based on the BC values in Table 3. The errors show the importance of the proposed method for estimating attitude in improving orbit and reentry predictions.

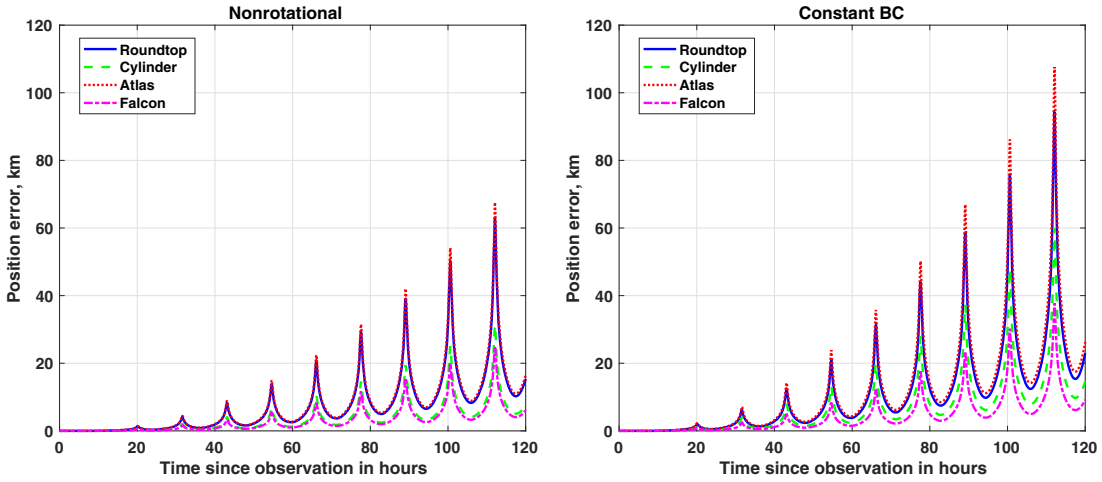

Fig. 12 Orbit propagation errors for all shape models. Left: nonrotational; right: constant BC.

VIII. Conclusions

In this paper, a nonlinear least-squares estimation scheme using light-curve measurements was presented and used to estimate the attitude and angular velocity of a resident space object with an assumed shape. This paper focused on rocket bodies with a perigee altitude lower than 300 km. The shape models consisted of triangular facets to allow for the modeling of complex rocket body shapes. Four different rocket body models were used: a simple cylinder, a simple cylinder with a rounded top, a Falcon 9 upper stage, and an Atlas upper stage. The light-curve model used was based on the Ashikhmin–Shirley BRDF and showed good performance for the simulated examples.

The estimated orientation trajectories were used to estimate the drag coefficient of the resident space object below 1000 km altitude over several orbits. Orbits are propagated with drag coefficients computed using the attitude variations, a constant attitude, and a constant drag coefficient to represent the typically used fitted ballistic coefficients. Results show that the orbit error can be on the order of tens of kilometers after just ten passes below 1000 km for a highly elliptical orbit. The errors highlight the importance of attitude knowledge in accurately predicting the orbits for collision avoidance and the significance of the method developed for its estimation.

As has been shown in this paper, the knowledge of attitude variations can significantly improve estimates of the drag acceleration that can in turn improve the correction estimated for the reference density model. This idea will be explored as part of future work. In addition, the more accurate expected estimates of the density derived from orbital decay of RSOs using the orientation trajectories can also provide data for improved dynamic calibration of the atmosphere, as in the case of HASDM. This idea will also be explored as part of future work.

Appendix: Attitude Dynamics Model

The attitude matrix in terms of the quaternion is given as

$$A(\boldsymbol{q}) = \Xi^T(\boldsymbol{q})\Psi(\boldsymbol{q}) \tag{A1}$$

where

$$\Xi(\boldsymbol{q}) \equiv \begin{bmatrix} q_4 I_{3\times3} + [\boldsymbol{\varrho}\times] \\ -\boldsymbol{\varrho}^T \end{bmatrix} \tag{A2a}$$

$$\Psi(\boldsymbol{q}) \equiv \begin{bmatrix} q_4 I_{3\times3} - [\boldsymbol{\varrho}\times] \\ -\boldsymbol{\varrho}^T \end{bmatrix} \tag{A2b}$$

with

$$[\boldsymbol{a}\times] \equiv \begin{bmatrix} 0 & -a_3 & a_2 \\ a_3 & 0 & -a_1 \\ -a_2 & a_1 & 0 \end{bmatrix} \tag{A3}$$

for any general 3×1 vector $\boldsymbol{a}$ defined such that $[\boldsymbol{a}\times]\boldsymbol{b} = \boldsymbol{a} \times \boldsymbol{b}$. This representation is constrained since the quaternion is of unit length and therefore $\boldsymbol{q}^T\boldsymbol{q} = 1$. The kinematics dynamics are given by a first-order differential equation as

$$\dot{\boldsymbol{q}} = \frac{1}{2}\Xi(\boldsymbol{q})\boldsymbol{\omega}_r \tag{A4a}$$

$$\dot{\boldsymbol{\omega}}^B_{rB/I} = J^{-1}\left(-\left[\boldsymbol{\omega}^B_{rB/I}\times\right]J\boldsymbol{\omega}^B_{rB/I}\right) \tag{A4b}$$

where J is the inertia matrix.

Under the small angle approximation, the rotational dynamics can be linearized by considering the first-order terms as [18]

$$\delta\dot{\boldsymbol{\xi}} = -\left[\hat{\boldsymbol{\omega}}^B_{rB/I}\times\right]\delta\boldsymbol{\xi} + \boldsymbol{\omega}^B_{rB/I} \tag{A5a}$$

$$\dot{\boldsymbol{\omega}}^B_{rB/I} = J^{-1}\left(-\left[J\hat{\boldsymbol{\omega}}^B_{rB/I}\times\right] + \left[\hat{\boldsymbol{\omega}}^B_{rB/I}\times\right]J\right)\boldsymbol{\omega}^B_{rB/I} \tag{A5b}$$

where $\hat{\boldsymbol{\omega}}^B_{rB/I}$ is the true angular velocity about which the equations are linearized. The state transition matrix for a time step of Δt can be calculated using the previously mentioned linearized equations with a matrix exponential. Equation (A5) can then be written in state space form as

$$\begin{bmatrix} \delta\dot{\boldsymbol{\xi}} \\ \dot{\boldsymbol{\omega}}^B_{rB/I} \end{bmatrix} = \underbrace{\begin{bmatrix} -[\hat{\boldsymbol{\omega}}^B_{rB/I}\times] & I_{3\times3} \\ 0_{3\times3} & (-[J\hat{\boldsymbol{\omega}}^B_{rB/I}\times] + [\hat{\boldsymbol{\omega}}^B_{rB/I}\times]J) \end{bmatrix}}_{F}\begin{bmatrix} \delta\boldsymbol{\xi} \\ \boldsymbol{\omega}^B_{rB/I} \end{bmatrix} \tag{A6}$$

The linearized dynamics matrix F computed at the time of each measurement is used to calculate the state transition matrix between t_k and t_{k-1}. In general, F can vary with time between t_{k-1} and t_k; however, it is assumed constant in this paper since the time step Δt is expected to be small. Therefore, the state transition matrix for the dynamic state can be given as

$$\boldsymbol{\Phi}(t_k, t_{k-1}) = \exp\{F(t_{k-1})\Delta t\} \tag{A7}$$

where $F(t_{k-1})$ is linearized about the time of the previous measurement allowing for the state transition matrix to be calculated as

$$\boldsymbol{\Phi}(t_k, t_0) = \prod_{i=1}^{k}\boldsymbol{\Phi}(t_i, t_{i-1}) \tag{A8}$$

Acknowledgments

The authors gratefully acknowledge the support of the U.S. Department of Energy through the Los Alamos National Laboratory/ Laboratory Directed Research & Development Program for this paper.

References

[1] Wetterer, C. J., and Jah, M. K., "Attitude Determination from Light Curves," *Journal of Guidance, Control, and Dynamics*, Vol. 32, No. 5, 2009, pp. 1648–1651. doi:10.2514/1.44254

[2] Linares, R., Jah, M. K., Crassidis, J. L., and Nebelecky, C. K., "Space Object Shape Characterization and Tracking Using Light Curve and Angles Data," *Journal of Guidance, Control, and Dynamics*, Vol. 37, No. 1, 2014, pp. 13–25. doi:10.2514/1.62986

[3] Linares, R., and Crassidis, J. L., "Space Object Shape Inversion via Adaptive Hamiltonian Markov Chain Monte Carlo," *Journal of Guidance, Control, and Dynamics*, Vol. 41, No. 1, 2018, pp. 47–58. doi:10.2514/1.G002296

[4] Linares, R., Jah, M. K., Crassidis, J. L., Leve, F. A., and Kelecy, T., "Astrometric and Photometric Data Fusion for Inactive Space Object Feature Estimation," *Acta Astronautica*, Vol. 99, June–July 2014, pp. 1–15. doi:10.1016/j.actaastro.2013.10.018

[5] Linares, R., Leve, F. A., Jan, M. K., and Crassidis, J. L., "Space Object Mass Specific Inertia Matrix Estimation from Photometric Data," *Advances in the Astronautical Sciences*, Vol. 144, 2012, pp. 41–54.

[6] Coder, R. D., Holzinger, M. J., and Linares, R., "Three-Degree-of-Freedom Estimation of Agile Space Objects Using Marginalized Particle Filters," *Journal of Guidance, Control, and Dynamics*, Vol. 41, No. 2, 2018, pp. 388–400. doi:10.2514/1.G001980

[7] Coder, R. D., Wetterer, C. J., Hamada, K. M., Holzinger, M. J., and Jah, M. K., "Inferring Active Control Mode of the Hubble Space Telescope Using Unresolved Imagery," *Journal of Guidance, Control, and Dynamics*, Vol. 41, No. 1, 2018, pp. 164–170. doi:10.2514/1.G002223

[8] Kaasalainen, M., and Torppa, J., "Optimization Methods for Asteroid Lightcurve Inversion I: Shape Determination," *Icarus*, Vol. 153, No. 1, 2001, pp. 24–36. doi:10.1006/icar.2001.6673

[9] Kaasalainen, M., and Torppa, J., "Optimization Methods for Asteroid Lightcurve Inversion II: The Complete Inverse Problem," *Icarus*, Vol. 153, No. 1, 2001, pp. 37–51. doi:10.1006/icar.2001.6674

[10] Calef, B., Africano, J., Birge, B., Hall, D., and Kervin, P. W., "Photometric Signature Inversion," *Proceedings of the International Society for Optical Engineering*, Vol. 6307, San Diego, CA, 2006, Paper 11, http://www.spie.org/Publications/Proceedings/Paper/10.1117/12.683015. doi:10.1117/12.683015

[11] Aeronautics, S. E., "Board, Continuing Keplers Quest: Assessing Air Force Space Commands Astrodynamics Standards, Committee for the Assessment of US Air Forces Astrodynamic Standards," Tech. Rept., National Research Council, National Academy Press, Washington D.C., 2012. doi:10.17226/13456

[12] Cook, G. E., "Satellite Drag Coefficients," *Planetary and Space Sciences*, Vol. 13, No. 10, 1965, pp. 929–946. doi:10.1016/0032-0633(65)90150-9

[13] Picone, J. M., Hedin, A. E., and Drob, D. P., "NRLMSISE-00 Empirical Model of the Atmosphere: Statistical Comparisons and Scientific Issues," *Journal of Geophysical Research*, Vol. 107, No. A12, 2002, pp. 2156–2202. doi:10.1029/2002JA009430

[14] Storz, M. F., Bowman, B. R., Branson, J. I., Casali, S. J., and Tobiska, W. K., "High Accuracy Satellite Drag Model (HASDM)," *Advances in Space Research*, Vol. 36, No. 12, 2005, pp. 2497–2505. doi:10.1016/j.asr.2004.02.020

[15] Ridley, A. J., Deng, Y., and Toth, G., "The Global Ionosphere Thermosphere Model," *Journal of Atmospheric and Solar–Terrestrial Physics*, Vol. 68, No. 8, 2006, pp. 839–864. doi:10.1016/j.jastp.2006.01.008

[16] Richmond, A. D., Ridley, E. C., and Roble, R. G., "A Thermosphere/ Ionosphere General Circulation Model with Coupled Electrodynamics," *Geophysical Research Letters*, Vol. 19, No. 6, 1992, pp. 601–604. doi:10.1029/92GL00401

[17] Marquardt, D. W., "An Algorithm for Least-Squares Estimation of Nonlinear Parameters," *Journal of the Society for Industrial and Applied Mathematics*, Vol. 11, No. 2, 1963, pp. 431–441. doi:10.1137/0111030

[18] Crassidis, J. L., and Junkins, J. L., *Optimal Estimation of Dynamic Systems*, CRC Press, Boca Raton, FL, 2011, pp. 184–189, 1011–1015.

[19] Schaaf, S. A., and Chambre, P. L., *Flow of Rarefied Gases*, Princeton Univ. Press, Princeton, NJ, 1961, pp. 38–47.

[20] Sentman, L., *Free Molecule Flow Theory and its Application to the Determination of Aerodynamic Forces, LMSC-448514*, Lockheed Missiles and Space Co., Lockheed Aircraft Corp., Sunnyvale, CA, 1961, pp. 3-1–3-32, http://books.google.com/books?id=H5HpHAAACAAJ.

[21] Mehta, P. M., McLaughlin, C. A., and Sutton, E. K., "Drag Coefficient Modeling for Grace Using Direct Simulation Monte Carlo," *Advances in Space Research*, Vol. 52, No. 12, 2013, pp. 2035–2051. doi:10.1016/j.asr.2013.08.033

[22] Mehta, P. M., Walker, A., Lawrence, E., Linares, R., Higdon, D., and Koller, J., "Modeling Satellite Drag Coefficients with Response Surfaces," *Advances in Space Research*, Vol. 54, No. 8, 2014, pp. 1590–1607. doi:10.1016/j.asr.2014.06.033

[23] Ashikmin, M., and Shirley, P., "An Anisotropic Phong BRDF Model," *Journal of Graphic Tools*, Vol. 5, No. 2, 2000, pp. 25–32. doi:10.1080/10867651.2000.10487522

[24] Wetterer, C. J., Linares, R., Crassidis, J. L., Kelecy, T. M., Ziebart, M. K., Jah, M. K., and Cefola, P. J., "Refining Space Object Radiation Pressure Modeling with Bidirectional Reflectance Distribution Functions," *Journal of Guidance, Control, and Dynamics*, Vol. 37, No. 1, 2014, pp. 185–196. doi:10.2514/1.60577

[25] Crassidis, J. L., Markley, F. L., and Cheng, Y., "Survey of Nonlinear Attitude Estimation Methods," *Journal of Guidance, Control, and Dynamics*, Vol. 30, No. 1, 2007, pp. 12–28. doi:10.2514/1.22452

[26] Hart, K. A., Dutta, S., Simonis, K., Steinfeldt, B. A., and Braun, R. D., "Analytically Derived Aerodynamic Force and Moment Coefficients of Resident Space Objects in Free-Molecular Flow," *AIAA SciTech, AIAA Atmospheric Flight Mechanics Conference*, AIAA Paper 2014-0728, 2014. doi:10.2514/6.2014-0728

[27] Walker, A., Mehta, P. M., and Koller, J., "A Quasi Specular Drag Coefficient Model Using the Cercignani Lampis Lord Gas Surface Interaction Model," *Journal of Spacecraft and Rockets*, Vol. 51, No. 5, 2014, pp. 1544–1563. doi:10.2514/1.A32677

[28] Goodman, F. O., "Preliminary Results of Three-Dimensional Hard Sphere Theory of Scattering of Gas Atoms from a Solid Surface," *Proceedings of the 5th International Symposium on Rarefied Gas Dynamics*, Academic, New York, 1977, pp. 35–48. doi:10.1016/0039-6028(67)90029-5

[29] Cercignani, C., and Lampis, M., "Kinetic Models for Gas Surface Interactions," *Transport Theory and Statistical Physics*, Vol. 1, No. 2, 1971, pp. 101–114. doi:10.1080/00411457108231440

[30] Comsa, G., Fremerey, J. K., Lindenau, B., Messer, G., and Röhl, P., "Calibration of a Spinning Rotor Gas Friction Gauge Against a Fundamental Vacuum Pressure Standard," *Journal of Vacuum Science and Technology*, Vol. 17, No. 2, 1980, pp. 642–644. doi:10.1116/1.570531

[31] Suetin, P. E., Porodnov, B. T., Chernjak, V. G., and Borisov, S. F., "Poiseuille Flow at Arbitrary Knudsen Numbers and Tangential Momentum Accommodation," *Journal of Fluid Mechanics*, Vol. 60, No. 3, 1973, pp. 581–592. doi:10.1017/S0022112073000352

[32] Porodnov, B. T., Suetin, P. E., Borisov, S. F., and Akinshin, V. D., "Experimental Investigation of Rarefied Gas Flow in Different Channels," *Journal of Fluid Mechanics*, Vol. 64, No. 3, 1974, pp. 417–438. doi:10.1017/S0022112074002485

[33] Mehta, P. M., Walker, A., McLaughlin, C. A., and Koller, J., "Comparing Physical Drag Coefficients Computed with Direct Simulation Monte Carlo Using Different Gas-Surface Interaction Models," *Journal of Spacecraft and Rockets*, Vol. 51, No. 3, 2014, pp. 873–883. doi:10.2514/1.A32566

[34] Kreyszig, E., *Advanced Engineering Mathematics*, 4th ed., Wiley, New York, 1979, pp. 880–885.

[35] Julier, S. J., and Uhlmann, J. K., "New Extension of the Kalman Filter to Nonlinear Systems," *Proceedings of SPIE*, Vol. 3068, 1997, pp. 182–193. doi:10.1117/12.280797

M. Grant
Associate Editor